13-17 June 2016, Washington, D.C. 8th AIAA Atmospheric and Space Environments Conference

AIAA AVIATION Forum



Fundamental Turbulence Measurement with Unmanned Aerial Vehicles

Brandon M. Witte,* Cornelia Schlagenhauf,† Jon Mullen,‡ Jacob P. Helvey,§ Michael A. Thamann¶, and Sean C.C. Bailey

Department of Mechanical Engineering, University of Kentucky, Lexington, KY, 40506, USA

This paper addresses the potential of using unamanned aerial vehicles for conducting fundamental research in the atmospheric boundary layer. A method of computing wind speed from a moving velocity sensor data is provided. The approach is demonstrated for both five-hole probes and hot-wire probes. Included in the procedure is an technique which was shown to provide an invertible, *a posteriori* calibration for hot-wire voltage data, demonstrated using data from a mid-afternoon flight of an unmanned aerial vehicle equipped with a single-sensor hot-wire probe. Several bulk and small-scale characteristics from small, fixed-wing unmanned aerial vehicle flights in the convective boundary layer are calculated, and show the potential for extracting a range of both large-scale and small-scale turbulence statistics.

I. Introduction

By acting as the boundary to the atmosphere, the earth's surface introduces forcing into it through frictional drag, evaporation and transpiration, heat transfer, pollutant emission and surface geometry. These interactions produce the highly turbulent atmospheric boundary layer (ABL), the lowest 200 m to 2000 m of the atmosphere, separated from the free atmosphere above it by the capping inversion which prevents mixing and dampens turbulence. Turbulence production in the ABL occurs through a balance of shear stress introduced by the surface and by buoyancy effects introduced by surface heat flux through temperature and humidity gradients. These buoyancy effects, subject to the diurnal cycle, produce stable, neutral, and unstable conditions within the ABL which typically evolve with time scales on the order of one hour [1].

The efficiency of the turbulence produced within the ABL for transporting heat, mass and momentum drives its response to surface forcing and accelerates the exchange of these quantities between the surface and atmosphere. Turbulence is therefore a crucial component of atmospheric boundary layer physics and it is the complexity of turbulence, its dynamics and internal interactions, which limits our understanding of the important transport processes which occur within it.

To understand turbulent phenomena, obtaining a spatial description of the structure and organization of the turbulence is of primary theoretical interest, particularly in the form of wavenumber spectra and spatial correlations. However, in spatially resolved ABL measurements the spatial resolution is relatively poor (i.e. through LIDAR measurements whose resolution is typically 10s of meters) relative to the Kolmogorov scale in the ABL (on the order of millimeters). Turbulence data is therefore frequently obtained in the form of temporal information through cup and sonic anemometers, which themselves only have temporal response of only 1-2 Hz [2] and 20 Hz respectively and spatial resolution of 10s of centimeters.

The use of unmanned aerial vehicles (UAVs) to conduct measurements in the ABL represents new possibilities for obtaining a spatial description of the structure and organization of turbulence. The ability of a UAV to spatially sample the flow field using a high temporal response sensor translates into a spatially sampled flow field with reduced reliance on Taylor's flow hypothesis. In addition, within the 30 minute period of quasi-stationarity within the ABL [1] a UAV will be able to collect substantially more data than a fixed-point measurement which requires the turbulence to convect past the measurement point. Finally, a UAV also has an advantage over fixed towers in terms of portability and the potential to measure in locations where construction of a tower is prohibitive.

Manned aircraft have been used to conduct atmospheric research for decades, conducting weather reconnaissance; measuring mean wind, temperature and humidity profiles; [3–5] measuring atmospheric turbulence; [6] and tracking pollutant concentrations. [7] In addition to atmospheric research, several pioneering studies in fundamental high

^{*}Graduate Student, Department of Mechanical Engineering, 151 R.G. Anderson Bldg.

[†]Visiting Student. Karlsruher Institut für Technologie Fakultät für Maschinenbau, 76128 Karlsruhe, Karlsruhe, Germany

[‡]Present address. Automated Driving, Ford Motor Company, 3200 Hillview Ave., Palo Alto, CA 94304

[§]Present address. Polypack Inc. 3301 Gateway Centre Blvd, Pinellas Park, FL 33782

[¶]Present address. General Atomics, 9779 Yucca Rd., Adelanto, CA 92301

Associate Professor, Department of Mechanical Engineering, 151 R.G. Anderson Bldg; sean.bailey@uky.edu; corresponding author

Reynolds number turbulence have also been performed using manned aircraft, [8, 9] towed sensors [10] and autonomous underwater vehicles. [11–13] UAVs offer distinct advantages over manned aircraft, however, in their ability to safely perform measurements within meters of the surface and through greatly reduced operational costs. [14]

Despite this potential, the use of UAVs for atmospheric turbulence research is still in its infancy, largely focusing on remotely piloted measurements of temperature, wind and humidity profiles [15, 16] with autonomous measurements rare [17–19] and employing wind velocity probes with temporal response little better than that of sonic anemometers. For example, Mayer et al. [20] have developed a UAV with meteorological equipment that estimates the wind vector by applying constant throttle and measuring the ground speed. Data are sampled at 2 Hz, for a wavenumber of 0.11 m⁻¹ at the maximum speed 18 m/s. The M2AV UAV developed by van den Kroonenberg et al. [18, 19] uses a five-hole Pitot tube which can resolve to 40 Hz, or 1.82 m⁻¹ at 22 m/s. Thomas et al. also use a five-hole Pitot tube equipped UAV to measure wind speed, wind direction, potential temperature, and water vapor flux[21].

In this paper, we demonstrate the feasibility of conducting atmospheric turbulence measurements using an unmanned aerial vehicles equipped with a hot-wire probe as well as present initial results from UAV flights utilizing five-hole probes. Hot-wire probes are a well-established measurement technique commonly employed in laboratory studies of turbulence due to their ability to provide frequency response $\mathcal{O}(10^4)$ kHz. Thus a UAV translating through the atmosphere at velocities $\mathcal{O}(10)$ m/s can potentially spatially resolve wavelengths in the atmosphere on the order of the Kolmogorov scale [1]. Single-sensor hot-wire probes, however, are only able to sense a single component of velocity. Thus, use of a five-hole probe in concert with a five-hole probe enables the investigation of the large-scale anisotropic turbulent structures through the determination of all three velocity components. In Section II we present a method of extracting wind velocity from the on-board sensors' velocity signals which is then applied to two test flights described in Section IV.

II. Data reduction

The objective of the measurements is to extract the wind velocity using a velocity signal measured by a multi-hole pressure probe or hot-wire sensor mounted on a vehicle which will be experiencing six degree-of-freedom rotation and translation. We assume the general configuration of the aircraft illustrated in Fig. 1 equipped with a velocity sensor aligned with the vehicle axis but mounted a distance from the center of gravity of the vehicle where r_{S-CG} denotes the vector that points from the center of gravity to the measurement volume of the respective wind sensor. We assume that the vehicle is equipped with a true air speed (TAS) sensor such as a Pitot-static tube. We also assume that the vehicle is equipped with an inertial navigation system or sensors, located at or near the center of gravity, which can determine the translational position and velocity, r_{UAV} and U_{UAV} respectively. In addition we assume that the rotational position, indicated through the Euler angles of pitch, roll and yaw (θ, ϕ) and ψ respectively) and the angular velocity Ω_{UAV} are provided by the autopilot. Thus, the time-varying position and orientation of the vehicle are known. It is noted that $[\cdot]_I$ denotes a vector in the earth-fixed inertial frame, and $[\cdot]_B$ is used to denote a vector in the vehicle-fixed body frame.

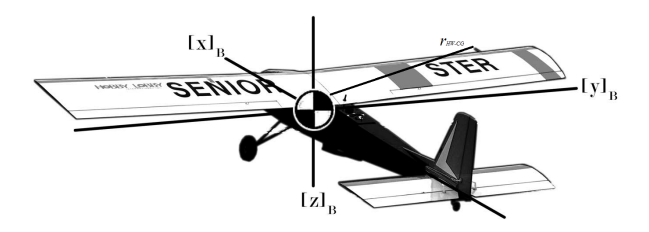


Figure 1. Standard airplane body axes.

To isolate the wind vector from the sensor measurements, we first note that the traveling probes will also sense the velocity of the plane relative to the velocity of the air in the atmosphere. Therefore, define the recorded relative velocity

$$[\boldsymbol{U}_r]_B = [\boldsymbol{U}_S]_B - [\boldsymbol{W}]_B \tag{1}$$

where $U_S = [u_1 \ u_2 \ u_3]^T$ is the velocity of the sensing volume and $W = [w_1 \ w_2 \ w_3]^T$ is the velocity of the atmosphere, i.e., the wind. The components of the inertial frame are taken as north, east and down. The components of the body frame are shown in Figure 1. Since the sensors face forward, it follows that $U_r = [u_{r1} \ u_{r2} \ u_{r3}]^T$ are the components of relative velocity normal, tangential, and bi-normal to the sensor axis, and are thus the components of velocity measured by the respective sensor.

We start first with the general case in which the applied sensor is capable of resolving these three components of velocity, such as with a multi-hole pressure probe or a three- or four-wire hot-wire probe in which a suitable data reduction scheme (i.e. such as provided by Wittmer et. al [22] or Döbbeling et. al [23]) has been used used to convert the voltage measured by the anemometer into velocity magnitude and direction.

Let $[U_{UAV}]_I$ denote the velocity of the vehicle given by the vehicle's inertial navigation system and assume that this measurement is taken at the center of gravity. The velocity of the sensor in the body frame is given by

$$[U_S]_B = [u_1 \ u_2 \ u_3]^T = [U_{UAV}]_B + [\Omega \times r_{S-CG}]_B, \tag{2}$$

where $\Omega = [P \ Q \ R]^T$.

Next, recall that a vector in the inertial frame is transformed into the body frame by $[\cdot]_B = L_{BI}[\cdot]_I$, where

$$L_{BI} = \begin{bmatrix} C_{11} & C_{12} & C_{13} \\ C_{21} & C_{22} & C_{23} \\ C_{31} & C_{32} & C_{33} \end{bmatrix},$$

$$C_{11} = \cos \theta \cos \psi,$$

$$C_{12} = \cos \phi \sin \psi,$$

$$C_{13} = -\sin \theta,$$

$$C_{21} = \sin \phi \sin \theta \cos \psi - \cos \phi \sin \psi,$$

$$C_{22} = \sin \phi \sin \theta \sin \psi + \cos \phi \cos \psi,$$

$$C_{23} = \sin \phi \cos \theta,$$

$$C_{31} = \cos \phi \sin \theta \cos \psi + \sin \phi \sin \psi,$$

$$C_{32} = \cos \phi \sin \theta \sin \psi - \sin \phi \cos \psi,$$

$$C_{33} = \cos \phi \sin \theta \sin \psi - \sin \phi \cos \psi,$$

$$C_{33} = \cos \phi \cos \theta,$$

and ϕ , θ , and ψ are the roll, pitch, and yaw angles, respectively [24]. Similarly, a vector in the body frame is transformed into the inertial frame by $[\cdot]_I = \boldsymbol{L}_{IB}[\cdot]_B$, where $\boldsymbol{L}_{IB} = \boldsymbol{L}_{BI}^{\mathsf{T}} = \boldsymbol{L}_{BI}^{\mathsf{T}}$.

The desired wind velocity is that in the inertial frame $[\mathbf{W}]_I = [w_n \ w_e \ w_d]^T$, where w_n is the component of wind along the north axis and w_e is the component of wind along the east axis and w_d is the component of wind along the downward axis. The wind velocity in the body frame is then

$$[\mathbf{W}]_{B} = \mathbf{L}_{BI}[\mathbf{W}]_{I}$$

$$= \begin{bmatrix} C_{11}w_{n} + C_{12}w_{e} + C_{13}w_{d} \\ C_{21}w_{n} + C_{22}w_{e} + C_{23}w_{d} \\ C_{31}w_{n} + C_{32}w_{e} + C_{33}w_{d} \end{bmatrix}.$$
(4)

Combining (2) and (10) with (1) leads to

$$[W]_I = [U_{UAV}]_I + [\Omega]_I \times r_{S-CG} - L_{IB}[U_r]_B.$$
 (5)

Thus, the desired quantity $[W]_I$ can be determined from the measured velocities $[U_r]_B$, $[U_{UAV}]_I$, $[\Omega]_I$ and the known quantity r_{S-CG} .

In the case where the applied sensor is a multi-hole pressure probe, an additional transformation step to the reduction scheme is necessary. Typical calibration procedures for these probes will result in the sensor reporting the true airspeed along with the aircraft's angle of attack, α , and sideslip angle, β allowing for the calculation of all three components of velocity. The angle of attack and sideslip angle are used to transform the recorded relative velocity, U_r , into x, y, and z components using the transformation L_{BA} according to [19, 25] defined as

$$\boldsymbol{L_{BA}} = D^{-1} \begin{bmatrix} 1 \\ \tan \beta \\ \tan \alpha \end{bmatrix}, \tag{6}$$

where D is the normalization factor defined as

$$D = \sqrt{(1 + \tan^2 \alpha + \tan^2 \beta)}. (7)$$

The updated equation used to find the desired quantity $[W]_I$ when using the multi-hole pressure probe is thus

$$[\boldsymbol{W}]_{I} = [\boldsymbol{U}_{UAV}]_{I} + [\boldsymbol{\Omega}]_{I} \times \boldsymbol{r}_{s-CG} - \boldsymbol{L}_{IB}\boldsymbol{L}_{BA}[\boldsymbol{U}_{r}]_{A}. \tag{8}$$

where $[\cdot]_A$ denotes the additional aerodynamic coordinate system recorded by the multi-hole pressure probe.

We now consider the case where the applied sensor is a single-sensor hot-wire probe. A single-sensor hot-wire anemometer is sensitive to all three velocity components but has only a single scalar, the voltage E, as its output. Thus the velocity that is cooling the hot-wire is usually modeled as an effective velocity, u_e . This effective velocity is meant to reflect the contributions of the three components of relative velocity and account for directional sensitivity. It is therefore defined as

$$u_e^2 = u_n^2 + k^2 u_b^2 + h^2 u_t^2, (9)$$

where k and h are constants to be determined by calibration [26]. Note that here the hot-wire probe is assumed to be oriented with the sensing wire parallel to the x-y plane of the vehicle such that $[u_n \ u_t \ u_b]^T = [u_{r1} \ u_{r2} \ u_{r3}]^T$. Additional configurations can be treated through introduction of an additional transformation matrix.

The single-sensor probe is only capable of resolving the component of wind that is facing the vehicle. We let W denote the component of wind that is facing the UAV, and in general $W = W(W(t), \psi(t))$ assuming that the vehicle is traveling in a horizontal plane relative to the earth such that the only components of wind capable of being resolved are $[W]_I = [w_n \ w_e \ 0]^T$. We note Lenschow[27] gives a treatment of the vertical velocity using the angle-of-attack, which for a vehicle with no additional sensors is unmeasured (the case we consider here). The wind velocity in the body frame is then

$$[\mathbf{W}]_{B} = \mathbf{L}_{BI}[\mathbf{W}]_{I}$$

$$= \begin{bmatrix} C_{11}w_{n} + C_{12}w_{e} \\ C_{21}w_{n} + C_{22}w_{e} \\ C_{31}w_{n} + C_{32}w_{e} \end{bmatrix},$$
(10)

where

$$w_n = -\mathcal{W}\cos\psi,\tag{11}$$

$$w_e = -W\sin\psi. \tag{12}$$

Substituting (11) and (12) into (10) gives

$$[\mathbf{W}]_{B} = - \begin{bmatrix} \mathcal{W} \cos \theta \\ \mathcal{W} \sin \phi \sin \theta \\ \mathcal{W} \cos \phi \sin \theta \end{bmatrix}, \tag{13}$$

then substituting (2) and (13) into (1) yields

$$[\boldsymbol{U}_r]_B = \begin{bmatrix} u_1 \\ u_2 \\ u_3 \end{bmatrix} + \begin{bmatrix} \mathcal{W}\cos\theta \\ \mathcal{W}\sin\phi\sin\theta \\ \mathcal{W}\cos\phi\sin\theta \end{bmatrix},$$

$$= [u_n \ u_t \ u_b]^{\mathrm{T}}.$$
(14)

Combining (9) and (14) gives the effective velocity as a function of W,

$$u_e^2 = (\mathcal{W}\cos\theta + u_1)^2 + k^2(\mathcal{W}\cos\phi\sin\theta + u_3)^2 + h^2(\mathcal{W}\sin\phi\sin\theta + u_2)^2.$$
(15)

Next, we note that, 1) typically, $h^2 \sim O(10^{-1})$, and 2) for typical vehicle motion $\sin \phi \sin \theta$ and u_2 are small. Thus the third term of (15) is treated as negligible. Therefore (15) becomes

$$u_e^2 = (\mathcal{W}\cos\theta + u_1)^2 + k^2(\mathcal{W}\cos\phi\sin\theta + u_3)^2. \tag{16}$$

Next, King's Law relates the voltage and effective velocity through

$$\frac{E^2(t)}{T_w - T(t)} = A + B(u_e^2(t))^n, \tag{17}$$

where A, B, and n are unknown calibration constants, T_w is the sensor temperature and T is the air temperature which we assume is measured [28]. It is preferable that T(t) be measured using a sensor mounted on the vehicle.

Although it is possible to find the calibration constants A, B and n through a controlled ground-based calibration before flight, in many cases this may be impractical. It is thus desirable to also be able to find the calibration constants from the flight data. To do this we minimize the least-squares functional

$$S(A, B, n) = \sum_{i} E_{i}^{2} - A - B(u_{e,i}^{2})^{n},$$

$$= \sum_{i} E_{i}^{2} - A - B((\mathcal{W}\cos\theta + u_{1})^{2} + k^{2}(\mathcal{W}\cos\phi\sin\theta + u_{3})^{2})_{i}^{n}.$$
(18)

To complete the calibration, we form an estimate for W from the true airspeed, which we assume is measured by a sensor with much lower frequency response than the hot-wire, such that the low frequency content of $u_n \approx \text{TAS}$. Then, using (14) implies that

$$W \approx \frac{\text{TAS} - u_1}{\cos \theta}.$$
 (19)

Typically, $|\theta|$ is small and therefore the denominator of (19) is neither small nor negative. Substituting (19) into (18) gives

$$S = \sum_{i} E_i^2 - A - B\left(u_{e,a}^2\right)_i^n, \tag{20}$$

where $u_{e,a}^2 = \text{TAS}^2 + k^2((\text{TAS} - u_1)\cos\phi\tan\theta + u_3)^2$.

Once the least-squares problem (20) is solved, giving A, B, and n, we invert (17) to solve for $u_e^2(t)$,

$$u_e^2(t) = \left(\frac{E^2(t)/(T_w - T(t)) - A}{B}\right)^{1/n}.$$
 (21)

Finally, we solve (16) for W,

$$0 = a\mathcal{W}^2 + b\mathcal{W} + c - u_e^2,\tag{22}$$

where $a = \cos^2 \theta + k^2 \cos^2 \phi \sin^2 \theta$, $b = 2u_1 \cos \theta + 2k^2 u_3 \cos \phi \sin \theta$, $c = u_1^2 + k^2 u_3^2$, and u_e^2 is given by (21). The solutions of (22) are real if $b^2 - 4a(c - u_e^2) > 0$, or

$$\left(\frac{E^2 - A}{B}\right)^{(1/n)} > \frac{k^2(u_1 \cos \phi \sin \theta - u_3 \cos \theta)^2}{\cos^2 \theta + k^2 \cos^2 \phi \sin^2 \theta}.$$

We remark that the correct interpretation of the square root in the quadratic formula is positive.

III. Experiment Description

We now report on two test flights which were conducted using different velocity sensors. In the first test flight, a single sensor hot-wire was employed and used to obtain small-scale turbulence statistics by assuming homogeneity and isotropy at these scales. In the second test flight, a five-hole pressure probe was used to obtain information about the large-scale anisotropic turbulence.

Both test flights were conducted at the Lexington Model Airplane Club's airfield (LMAC), which is a grassy field and paved runway east of Lexington, KY, USA. The Bluegrass Airport (KLEX) is approximately 20 miles west of the airstrip, while the Mount Sterling-Montgomery County Airport (KIOB) is approximately 20 miles east of the airstrip.

A. UAV

1. Hot-wire probe flight

To demonstrate the feasibility of using a UAV to measure turbulence with a hot-wire probe, an experiment was conducted using a modified off-the-shelf Senior Telemaster remote-controlled aircraft manufactured by Hobby Lobby

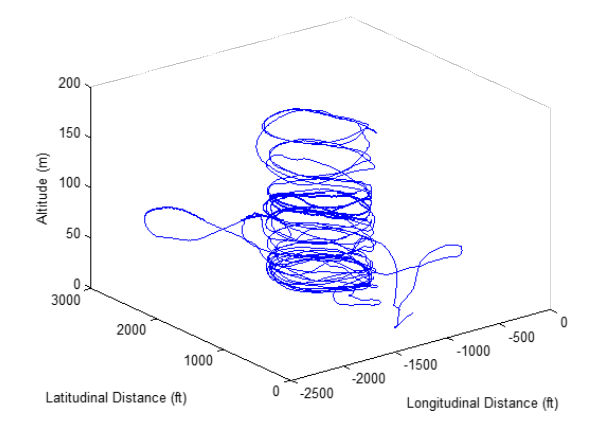


Figure 2. Flight path of test flight. The UAV conducted measurements at nine altitude-levels, flying in horizontal circles several times at each.

International, Inc. The aircraft was equipped with three 3300 mAh 4-cell lithium-polymer batteries in series and a NEU 1515-2Y DC motor for propulsion, producing a cruising speed of 20 m/s to 30 m/s.

The airframe was equipped with a Piccolo autopilot system which autonomously follows an updateable waypoint-based trajectory sent to it from a ground station. For position and orientation sensing, the autopilot was equipped with an inertial navigation system consisting of a three-axis accelerometer, three gyroscopes, and a global positioning system (GPS) transponder. Air data in the form of altitude and TAS for flight control is provided through an absolute pressure transducer and Pitot-static tube connected to a differential pressure transducer embedded within the autopilot. Telemetry was sent to the ground station through a radio frequency data link at a rate of 10 Hz. This telemetry data included full six degree-of-freedom position and velocity information.

The fluctuating velocity was measured using a single-sensor hot-wire probe with a 5 μ m diameter, 1 mm long Pt-Rh sensing element. The probe was driven by a TSI Model 1750 Constant-Temperature Anemometer at a temperature of $T_w \approx 350^{\circ}$ Cand mounted forward-facing on the left wing with the sensing element approximately parallel to the ground plane. The voltage output of the anemometer was filtered at 10 kHz using a simple RC analog filter and the frequency response of the probe estimated as > 10 kHz using a square-wave test before flight.

To measure the ambient temperature, an Omega TH-44008 thermistor with 2.5 second response time was used, installed in a simple Wheatstone bridge circuit. Humidity was also measured using an IST P14SMD capacitive humidity sensor (5 s response time), however the data from this sensor are not reported here. Two ADXL335 accelerometers (1 kHz bandwidth) were mounted in the wing, in-line with the hot-wire probe.

Data logging of the voltage output from the hot-wire, temperature, humidity and accelerations sensors was conducted at 20 kHz using a stand-alone high-speed Omega OM-LGR-5329 multifunction data logger (DAQ). All sensors and the data logger were powered by a single 20 V, 2200 mAh lithium-polymer battery.

Although data was acquired at 20 kHz, during post-processing of the data, it became apparent that there was a disproportionate amount of high frequency electrical noise contained in the signals of all-sensors. Hence, for the results presented here the hot-wire voltage was digitally low-pass filtered using a first-order, zero-lag Butterworth filter at 3 kHz.

This test flight was conducted in a late afternoon in August. At the start of this test flight KLEX reported, via the NOAA, a temperature of 32.2°C, wind at 2.6 m/s north, and scattered clouds. Towards the end of the flight 32.2°C, 4.1 m/s NNW, and partly cloudy was being reported by KLES and a temperature of 31.0°C, wind at 3.6 m/s NE, and scattered clouds was beingt reported by KIOB.

Due to the limited airspace available at LMAC, the flight plan was restricted to flying in a circular pattern at a near-constant altitude-level for 30-71 s at several altitudes. The flight path, shown in Fig. 2, is computed by integrating the UAV's velocity in an earth-fixed frame. Measurements were conducted at nine distinct altitude levels above ground, ranging from 18 m to 120 m.

2. Five-hole probe flight

The unmanned aerial vehicle used in the experiment to measure the large isotropic scales of turbulence with the five-hole pressure probe was customized off-the-shelf Skywalker X8 flying wing created by Skywalker Technologies. The

aircraft was powered by an AXi Gold 4120/14 DC motor with one 8000 mAh 4 cell lithium-polymer (LiPo) battery allowing for flight times of in excess of 45 minutes at cruise speeds of around 17 m/s.

In an attempt to decrease system costs, an open source Pixhawk autopilot was used and provided on board attitude and inertial measurements for the data reduction. Like the Piccolo this autopilot allows for the X8 to fly autonomously between predetermined waypoints. In addition to the five-hole pressure probe, a Pitot-static tube is used to provide TAS for flight control as well as a reference for cross-correlating the separate data systems on board. The six degree-of-freedom position, velocity, and GPS information is recorded on-board the autopilot at 50 Hz, 10 Hz, and 5 Hz respectively and downloaded after each flight.

The five-hole probe used for this experiment was a custom made instrument created using a desktop stereolithography (SLA) 3D Printer (Formlabs Form 1+). The five holes on the sensor were 1.2 mm in diameter and the tip of the probe supports a 30° tip angle. Each hole is connected to a ± 2 kPa differential pressure transducer (Freescale Semiconductor MPXV7002DP). The probe was mounted along the x-axis out of the nose of the aircraft to minimize any disturbances in the flow caused by the airframe.

The data logging of the voltage output from the transducers was completed using an MCC USB-1608FS-Plus data acquisition unit driven by a 2nd generation Raspberry Pi at 2 KHz for each channel. The sensors, Raspberry Pi, and DAQ were all powered by a 5V, 2200 mAh lithium-polymer battery. This data was then re-sampled to the 50 Hz frequency of the six degree-of-freedom information from the autopilot, itself aligned using the airspeed data from the additional Pitot-static tube on board.

The presented data for the five-hole probe are from a test flight conducted on a late afternoon in mid February. Temperatures reported by KLEX were 7° C with 4.5 m/s winds from the SE. The flight plan for the five-hole probe mission followed a circular loiter path with a radius of 60 meters at a single altitude of 100 meters.

B. Implementation of Data Reduction

To implement the data reduction method described in Section II from the test flights, we use inertial data from the respective autopilot for the UAV's velocities, Euler angles, and Euler angle rates. Due to a lack of calibration for the hot-wire's directionality, we assume the calibration constant k=1. Because the implementation of the data reduction scheme is identical between the two flights in respect to correlating the separate system's information, only the hot-wire implementation is discussed here.

The velocity probe data were sampled by the on-board data-acquisition system at frequency f_1 whereas the UAV velocities and Euler angles were recorded from the autopilot telemetry at frequency f_2 . Therefore, the initial data reduction step required alignment of the two sets of time series data. To perform this alignment, we first assume that the UAV position and orientation smoothly transitions between sample points in the telemetry data, allowing interpolation of the telemetry data from f_2 to f_1 using a cubic interpolation scheme. The relative time difference between the start of each set of time-series data was then determined by cross-correlating the acceleration data from the sensors recorded by the DAQ with the autopilot acceleration data recorded in the telemetry data. Identification of the location of maximum in the cross-correlation allowed determination of the relative shift between the initiation of sampling between the DAQ and telemetry data. As a result $[r_{\text{UAV}}(t_i)]_I$, $[U_{UAV}(t_i)]_I$, $[\Omega(t_i))]_I$ $L_{BI}(t_i)$ are known where t_i is the time corresponding to each discrete sample of velocity probe voltage, $E(t_i)$, and temperature, $T(t_i)$.

To ease convergence of the least-squares fit used for the hot-wire calibration, we filter both the hot-wire voltage $E(t_i)$ and the approximate effective velocity $u_{e,a}^2(t_i)$, and denote these $\widetilde{E}(t_i)$ and $\widetilde{u_{e,a}}^2(t_i)$ respectively. The calibration of A, B, and n is completed for each altitude-level by minimizing the least-squares functional (20), with \widetilde{E} substituted for E and $\widetilde{u_{e,a}^2}$ substituted for $u_{e,a}^2$. The fit for one altitude-level is shown graphically in Fig. 3. The results converged for each altitude-level and the results for n were found to be very close to the values of n between 0.40 and 0.55 typically found using similar probes and conventional calibration techniques [28].

With these values for A, B and n, $u_{e,a}(t_i)$ was determined through (21) and thus $W(t_i)$ through (22). Furthermore, knowing $[r_{UAV}(t_i)]_I$, the quantities $[W(x)]_I$ and $[T(x)]_I$ could be found.

IV. Results

A. Hot-wire probe flight

Whereas for a probe measuring three-components of velocity identifying the mean wind velocity and direction is relatively straightforward using the measured wind vector $\mathbf{W}(t)$, for a single-sensor hot-wire probe, extracting these quantities requires additional processing. However, the definition of $\mathcal{W}(t) = \mathcal{W}(\mathbf{W}(t), \psi(t))$ as the component of $\mathbf{W}(t)$ directed at the vehicle implies that $\mathcal{W}(t)$ is maximized when the UAV is facing into the wind. Therefore, we can find the mean wind speed by finding the maximum speed at each altitude-level. To eliminate influence from all

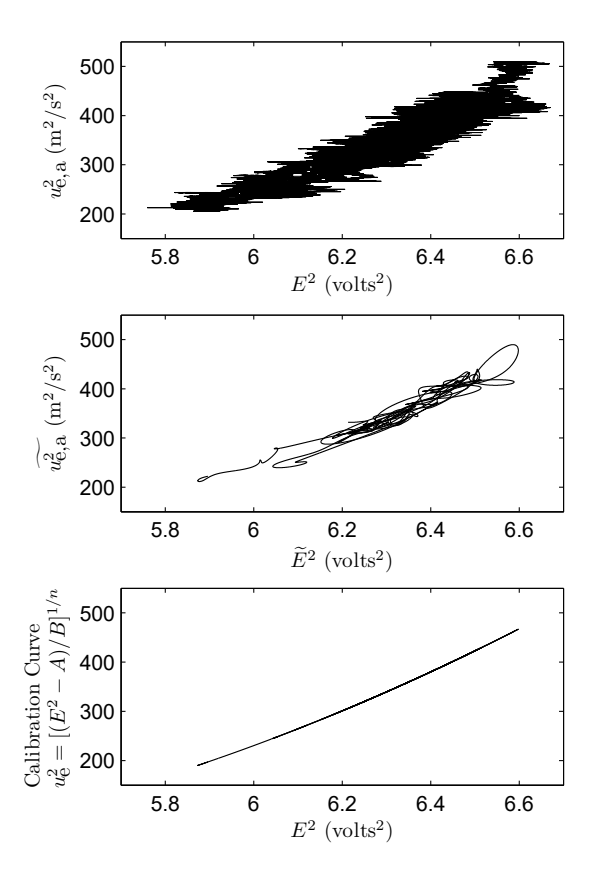


Figure 3. Example hot-wire calibration. The hot-wire voltage squared E^2 is calibrated against an approximate effective velocity $u_{\mathbf{e},\mathbf{a}}^2$ (top) using the least-squares functional (20). To ease convergence, in practice we use \widetilde{E}^2 and $\widetilde{u}_{\mathbf{e},\mathbf{a}}^2$ in place of E^2 and $u_{\mathbf{e},\mathbf{a}}^2$ (middle). For each altitude-level, the damped Newton iterations converge. Shown is the fifth altitude-level and its calibration (bottom).

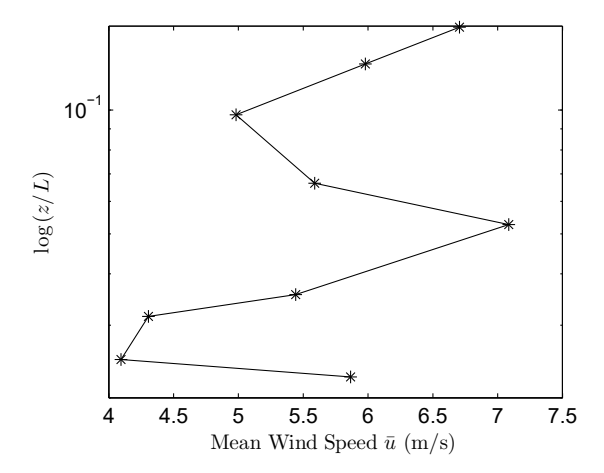


Figure 4. Mean wind speed. The mean wind speed is taken as the maximum filtered wind velocity recorded by the hot-wire. Based on weather data gathered nearby, these results are high.

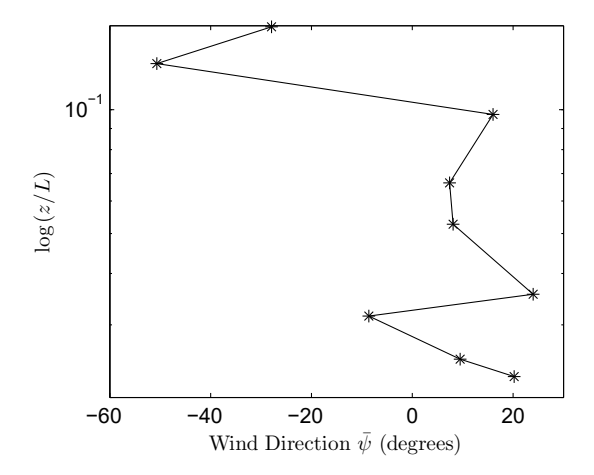


Figure 5. Wind direction. The wind direction $\overline{\psi}$ is taken as the direction in which the hot-wire records the maximum filtered wind velocity, where north is 0° . Based on weather data gathered nearby, these results are plausible.

but the slowest time-scales, we use a filtered wind speed, $\widetilde{\mathcal{W}}(t)$, which is filtered at 1 Hz using a fourth-order zero-lag Butterworth lowpass filter.

We can define the mean wind speed as $\overline{U}_i = \max_{t \in \mathcal{T}_i} \widetilde{\mathcal{W}}(t)$ and define $t_{\bar{\psi},i} \in \mathcal{T}_i$ such that $\widetilde{\mathcal{W}}(t_{\bar{\psi},i}) = \overline{U}_i$. We also let $z_i = \operatorname{mean}_{t \in \mathcal{T}_i} z(t)$. Here we non-dimensionalize the altitude z using the height of the convective boundary layer, which here we assume is L = 1 km[29]. Finally, we note that we can also find the mean wind direction $\overline{\psi}_i = \psi(t_{\bar{\psi},i})$ as the direction the vehicle is facing when \overline{U}_i is observed.

The measured mean wind speed is shown in Figure 4 with the wind direction, shown in Figure 5 and the results are within approximately 10% of that reported by the autopilot using the difference between TAS and ground speed.

The advantage of the hot-wire probe over most other commonly used velocity measurement tools is its temporal response, which allows it to temporally resolve the turbulence. On the traversing UAV, this temporal resolution translates to spatial sample resolution, allowing the measurement of turbulence over a range of spatial scales.

One quantity of primary interest is the Reynolds stress tensor $\rho \overline{u'u'}$ or often simply $\overline{u'u'}$, where ρ is the density, $u' = W(t) - \overline{W}$ and the overline indicates a time average. With the Reynolds stress tensor known, the turbulent kinetic energy can also be found, defined as

$$K = \frac{1}{2} \operatorname{Tr} \left(\mathbf{u}' \mathbf{u}' \right) \tag{23}$$

where Tr indicates the trace of the Reynolds stress tensor.

Although the Reynolds stress tensor can be readily obtained from three-component velocity measurements, for a

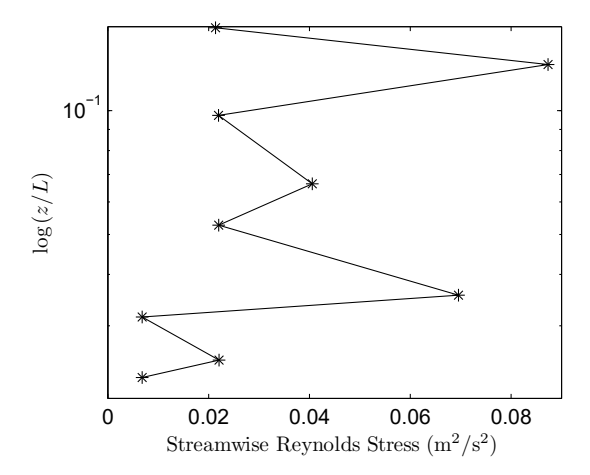


Figure 6. Turbulent kinetic energy. The turbulent kinetic energy is computed over a short time when the hot-wire is facing into the wind. The plot indicates increasing turbulence production by shear with increasing altitude.

single-sensor hot-wire, we instead must assume isotropy of the turbulence to obtain an estimate of turbulent kinetic energy. Through the assumption of approximate isotropy we can estimate K through

$$\widetilde{K} = \frac{3}{2} \overline{\mathcal{W}' \mathcal{W}'} \tag{24}$$

where $W' = W(t) - \overline{W}(t)$ and the overline indicates a time average.

The quantity K_i is computed at each altitude-level and the results are shown in Fig. 6.

The advantage of using a traversing probe mounted on a UAV is the ability to spatially sample the turbulence and therefore resolve the power spectrum of the turbulence in wavenumber space, without application of Taylor's frozen flow hypothesis. To compute the power spectral density in wavenumber space, we assume isotropy and use the entire time-series from each altitude-level. First, we compute the distance along the UAV's path at each altitude level,

$$r_i(t) = \int_{t_{1,i}}^{t+t_{1,i}} ||U_{HW}(\tau)|| d\tau.$$
 (25)

Next, we view the wind velocity as a function of $r_i(t)$, i.e. $\mathcal{W} = \mathcal{W}(r_i(t))$. In discrete time, the entries of $r_i(t)$ are monotonically increasing, but unevenly spaced. Therefore, we interpolate $r_i(t)$ and $\mathcal{W}(t)$ to the shortest distance step and compute the power spectral density. Due to the uneven spacing in r_i , there are wavenumbers that will appear resolved that are not. Thus, we define an effective Nyquist wavenumber as the Nyquist frequency of the DAQ divided by the maximum speed of the UAV. In the reported flight test, the effective Nyquist wavenumbers have range 342 m^{-1} to 406 m^{-1} , indicating possible resolution to 3 mm. An alternative, but computationally-intense, treatment for unevenly sampled data is given by Lomb [30].

We also note that an ideal flight path for estimating the power spectrum is that of a straight-line trajectory. The circular flight path used in the presented demonstration flights is unable to spectrally resolve eddies larger than the diameter of the orbit (~ 200 m, such that wavenumbers greater than ~ 1 m⁻¹ should be considered unreliable).

The power spectral density for three altitude-levels are shown in Fig. 7. All power spectral densities show agreement with Kolmogorov's -5/3 prediction for the inertial subrange over two or two and a half decades which shows that the spatially transformed turbulence spectrum in wavenumber space matches the expected inertial subrange. At high wavenumbers, $k > \sim 10^{-1}$ the electrical interference previously noted appears as a deviation from the -5/3 slope. This inaccuracy in the high-frequency content obscures what might be the beginning of the dissipation scale at approximately $k = 250 \text{ m}^{-1}$.

The time response of the hot-wire probe also allows estimation of the small-scale turbulent properties. To find the dissipation rate at each altitude-level, we again consider $W = W(r_i(t))$. Assuming isotropy, the dissipation rate can be estimated from single component velocity measurements using $\epsilon = 15\nu \overline{(\partial W/\partial r)^2}$ [31], where ν is kinematic viscosity. To compute $\partial W/\partial r$, we use second-order differencing. The results are shown in Fig. 8.

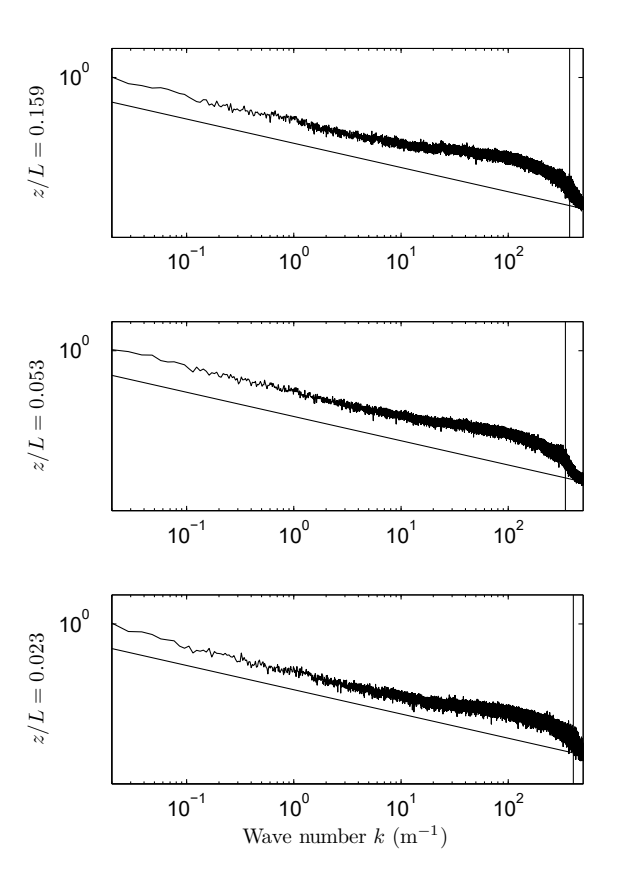


Figure 7. Power spectral density. The power spectral density of the wind is shown at three different altitudes. The diagonal line is Kolmogorov's -5/3 slope while the vertical line is the minimum Nyquist frequency. The power spectrum follows the -5/3 slope for at least two decades. Presumed inaccuracy in the high-frequency content obscures what might be the beginning of the dissipation scale at approximately $k=250~{\rm m}^{-1}$.

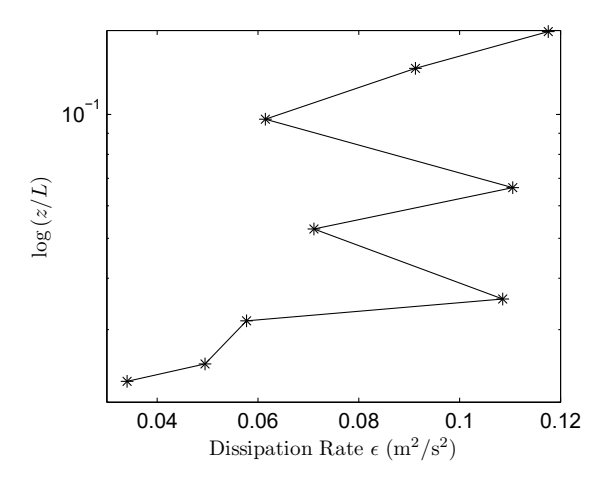


Figure 8. Dissipation Rate. The dissipation rate ϵ is computed by assuming isotropy and numerically differentiating $W=W(r_i(t))$. Like the streamwise Reynolds stress, the dissipation rate increases with increasing altitude.

With $\overline{W'W'}_i$ and ϵ_i known, it is also possible to estimate the Taylor microscale[31] using

$$\lambda_i = \left(\frac{\nu \overline{W'W'}_i}{\epsilon_i}\right)^{1/2},\tag{26}$$

which gives values of λ_i ranging 1.8-4.0 mm. We are also able to estimate the Kolmogorov scale,

$$\eta_i = \left(\frac{\nu^3}{\epsilon_i}\right)^{1/4},\tag{27}$$

which gives values of η_i ranging 0.4-0.6 mm. We remark that in the present measurements, neither λ_i nor η_i is fully resolved, and furthermore, they are in the range affected by the excessive high frequency content of the hot-wire anemometer signal. However, the agreement between the present estimates of these scales and the expected values [1] is promising.

B. Five-hole probe flight

With the five-hole probe data, the analysis is more focused on large-scale structure of the turbulence to minimize impact of the relatively low frequency response of pressure probes, while taking advantage of their ability to recover all three velocity components.

We first resolve the wind vector W into a velocity vector $U = [U_x \ U_y \ U_z]^T$ such that the mean wind is aligned with the streamwise component U_x , with the transverse component U_y and component U_z normal to the ground. We then focus on the perturbations from the mean, for example $u'(t) = U(t) - \overline{U}_x$ for the streamwise component. The resulting perturbation vector is shown overlaid on the flight track in Fig. 9a.

To remove time dependence of the data, we apply Taylor's frozen flow hypothesis [32] to translate temporal information into spatial information using \overline{U}_x as an advection velocity. The resulting spatial position is thus $x^* = x + \overline{U}_x t$ and the resulting vector field as a function of x^* is shown in Fig. 9b.

Examination of the transformed vector field of Fig. 9b reveals the signature of large-scale coherent motion in the form of large-scale regions of u' with similar sign. A commonly used approach to characterize the scale of coherent motions is the correlation function. Here, calculated through

$$R_{ij}(\boldsymbol{\Delta}\boldsymbol{x}) = \frac{\overline{u_i'(\boldsymbol{x})u_j'(\boldsymbol{x} + \boldsymbol{\Delta}\boldsymbol{x})}}{\overline{u_i'^2}^{1/2}\overline{u_j'^2}^{1/2}}$$
(28)

where Δx is a position displacement vector and the subscripts i and j can represent the x, y or z directions.

The autocorrelation R_{xx} is shown in Fig. 9c. This statistic was calculated using the Taylor-hypothesis-transformed flight track so that the velocity field can be assumed to be independent of time. The quantity $u_i'(x^*)u_j'(x^* + \Delta x)$ is determined for each point in transformed space where, to increase convergence of the statistics, points are included in the calculation if they are within the minimum selected value of Δx , for example 5 m.

The results shown in Fig. 9c show the characteristic signature of large-scale motion, with the elongated positive region flanked by two smaller regions of negative correlation [33]. However, it is also apparent from the variability observed away from the region of high correlation that the statistics are only marginally converged.

This lack of convergence is also evident in Fig 9d which shows the second and third order longitudinal structure functions, defined as

$$S_u^n(\Delta x) = \overline{\left[\left(u_x\left(\mathbf{x} + \Delta x\right) - u_x\left(\mathbf{x}\right)\right)\right]^n}$$
(29)

where n describes the order of the structure function and Δx is in the direction of u_x . Once Δx is is out of the dissipation range and within the inertial range, it can be observed that the general trend follows the expected exponential increase [34]. However, it is not possible to determine the value of the exponent of the structure function, as the statistics are not yet converged.

V. Conclusions

This paper presented an approach for extracting the wind velocity vector from velocity sensors mounted on a fixed wing UAV, focusing on multi-hole pressure probes and hot-wire probes. The procedure was shown to provide an invertible, *a posteriori* calibration for the hot-wire data using a co-located Pitot-static tube. Using data from two test flights, one with a hot-wire probe and one with a five-hole probe, several bulk and small-scale characteristics of the convective boundary layer were computed, and showed some agreement with weather measurements and expected

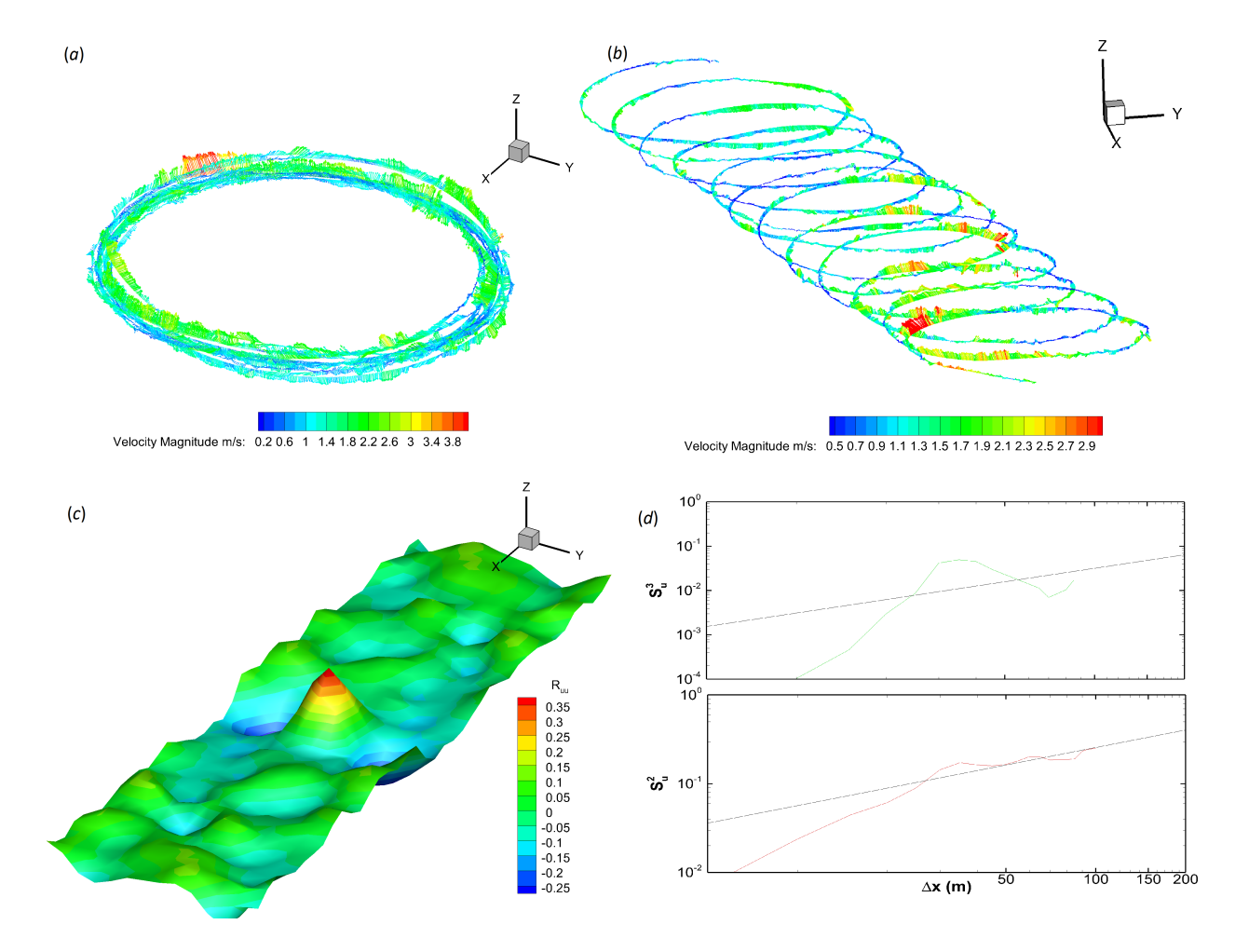


Figure 9. Five-hole probe results. The flight track and corresponding wind velocity vector is shown in (a) with the same data transformed using Taylor's frozen flow hypothesis shown in (b). The resulting autocorrelation of streamwise velocity is shown in (c) and longitudinal second and third order structure functions shown in (d).

results for the flight conditions. The small scale-statistics may have been skewed by excessive high frequency content of the hot-wire signal, and the large-scale statistics may have lacked convergence. However, the results presented here are still preliminary and therefore the results are quite promising for being able to obtain reliable statistics with refinement of the approach.

Current ongoing work is focusing on the improving the signal-to-noise ratio of the hot-wire measurements, and incorporating a secondary RTK GPS to obtain more precise to gain more precise position information, in order to resolve turbulent scales with sub-centimeter resolution. In addition, efforts are ongoing to improve the accuracy of the multi-hole pressure probe systems, quantify the frequency response of the custom probes, and conduct test flights with longer endurance in order to gain more accurate, resolved, large-scale statistics.

Acknowledgements

This work was supported by the National Science Foundation through grant #CBET-1351411 and by National Science Foundation award #1539070, Collaboration Leading Operational UAS Development for Meteorology and Atmospheric Physics (CLOUDMAP).

References

- [1] R.B. Stull. An Introduction to Boundary Layer Meteorology. Springer, 1988.
- [2] S. Yahaya and J.P. Frangi. Cup anemometer response to the wind turbulence measurement of the horizontal wind variance. *Annales Geophysicae*, 22:3363–3374, 2004.
- [3] D.H. Lenschow and W.B. Johnson. Concurrent airplane and balloon measurments of atmospheric boundary layer structure over a forest. *J. Appl. Meteor.*, 7:79–89, 1968.
- [4] W.M. Angevine, S.K. Avery, and J.L. Kok. Virtual heat flux measurements from a boundary-layer profiler-rass compared to aircraft measurements. *J. Appl. Meteor.*, 32:19011907, 1993.
- [5] C.R. Philbrick. Raman lidar descriptions of lower atmosphere processes. In *Proceedings of the 21st ILRC, Valcartier, Quebec Canada*, page 535545, 2002.
- [6] W.L. Eberhard, R.E. Cupp, and K.R. Healey. Doppler lidar measurement of profiles of turbulence and momentum flux. *J. Atmos. Oceanic Technol.*, 6:809–819, 1989.
- [7] V. Matvev, U. Dayan, I. Tass, and M. Peleg. Atmospheric sulfur flux rates to and from israel. *The Science of the Total Environment*, 291:143–154, 2002.
- [8] F.R. Payne and J.L. Lumley. One-dimensional spectra derived from an airborne hot-wire anemometer. *Quarterly Journal of the Royal Meteorological Society*, 92:397–401, 1966.
- [9] C. M. Sheih, H. Tennekes, and J.L. Lumley. Airborne hot-wire measurements of the small-scale structure of atmospheric turbulence. *Phys. Fluids*, 14(2):201–215, 1971.
- [10] H. L. Grant, R. W. Stewart, and A. Moilliet. Turbulence spectra from a tidal channel. J. Fluid Mech., 12:241-268, 1962.
- [11] M.R. Dhanak and K. Holappa. An autonomus ocean turbulence measurement platform. *Journal of Atmospheric and Oceanic Technology*, 16:1506–1518, 1999.
- [12] E. R. Levine and R.G. Lueck. Turbulence measurements from an autonomous underwater vehicle. *Journal of Atmospheric and Oceanic Technology*, 16:1533–1544, 1999.
- [13] S. A. Thorpe, T. R. Osborn, J. F. E. Jackson, J. Hall, and R. G. Lueck. Measurements of turbulence in the upper-ocean mixing layer using Autosub. *Journal of Physical Oceanography*, 33:122–145, 2003.
- [14] S. Metzger, W. Junkermann, K. Butterbach-Bahl, H. P. Schmid, and T. Foken. Measuring the 3-d wind vector with a weight-shiftmicrolight aircraft. *Atmos. Meas. Tech.*, 4:1421–1444, 2011.
- [15] J. Egger, S. Bajrachaya, R. Heingrich, P. Kolb, S. Lammlein, M. Mech, J. Reuder, W. Schäper, P. Shakya, J. Shween, and Wendt. H. Diurnal winds in the himalayan kali gandaki valley. part iii: Remotely piloted aircraft soundings. *Mon. Wea. Rev.*, 130:2042–2058, 2002.
- [16] S. Hobbs, D. Dyer, D. Courault, A. Olioso, J.-P. Lagouarde, Y. Kerr, J. McAnneney, and J. Bonnefond. Surface layer profiles of air temperature and humidity measured from unmanned aircraft. *Agronomie*, 22(6):635–640, 2002.

- [17] C. Eheim, C. Dixon, B.M. Agrow, and S. Palo. Tornado chaser: A remotely-piloted UAV for in situ meteorological measurements. In AIAA Paper 2002-3479, 1st AIAA Unmanned Aerospace Vehicles, Systems, Technologies, and Operations Conference and Workshop, 2002.
- [18] A.C. van den Kroonenberg, T. Spieß, M. Buschmann, T. Martin, P.S. Anderson, F. Beyrich, and J. Bange. Boundary layer measurements with the autonomous mini-UAV M²AV. In *Proceedings of DACH2007*, Hamburg, Germany, 2007.
- [19] A. van den Kroonenberg, T. Martin, M. Buschmann, J. Bange, and P. Vörsmann. Measuring the wind vector using the autonomous mini aerial vehicle M²AV. J. Atmos. Oceanic Technol., 25:1969–1982, 2008.
- [20] S Mayer, M Jonassen, A Sandvik, and J Reuder. Atmospheric profiling with the UAS SUMO: a new perspective for the evaluation of fine-scale atmospheric models. *Meteorology and Atmospheric Physics*, 116(1–2):15–26, 2012.
- [21] R M Thomas, K Lehmann, H Nguyen, D L Jackson, D Wolfe, and V Ramanathan. Measurement of turbulent water vapor fluxes using a lightweight unmanned aerial vehicle system. Atmos. Meas. Tech, 5:5529–5568, 2012.
- [22] K.S. Wittmer, W.J. Devenport, and J.S. Zsoldos. A four-sensor hot-wire probe system for three-component velocity measure-ment. Exp. Fluids, 24:416–423, 1998.
- [23] K. Döbbeling, B. Lenze, and W. Leuckel. Computer-aided calibration and measurements with quadruple hotwire probes. *Exp. Fluids*, 8:257–262, 1990.
- [24] Bernard Etkin. Dynamics of Atmospheric Flight. Dover Publications, 2000.
- [25] D. N. Axford. On the accuracy of wind measurements using an inertial platform in an aircraft, and an example of a measurement of the vertical mesostructure of the atmosphere. *Journal of Applied Meteorology*, 7(4):645–666, 1968.
- [26] H. H. Bruun. Hot-wire Anemometry. Oxford University Press, Oxford, UK, 1995.
- [27] D H Lenschow. Airplane measurements of planetary boundary layer structure. *Journal of Applied Meteorology*, 9(6):874–884, 1970.
- [28] S. Tavoularis. Measurement in Fluid Mechanics. Cambridge University Press, 2005.
- [29] John L Lumley and Hans A Panofsky. The Structure of Atmospheric Turbulence. Wiley, 1964.
- [30] N R Lomb. Least-squares frequency analysis of unequally spaced data. Astrophysics and Space Science, 39(2):447–462, 1976.
- [31] H. Tennekes and J. L. Lumley. A First Course in Turbulence. The MIT Press, Cambridge, Massachusetts, 1972.
- [32] G. I. Taylor. The spectrum of turbulence. Proc. R. Soc. Lond., 164(919):476–490, 1938.
- [33] S. C. C. Bailey and A. J. Smits. Experimental investigation of the structure of large- and very-large-scale motions in turbulent pipe flow. *J. Fluid Mech.*, 651:339–356, 2010.
- [34] U. Frisch and M. Vergassola. A prediction of the multifractal model: the intermediate dissipation range. *Europhys. Lett.*, 14:439–444, 1991.